Left Atrium Pulmonary Veins: Segmentation and Quantification for Planning Atrial Fibrillation Ablation

R. Karim[a], R. Mohiaddin[b] and D. Rueckert[c]

[a,c]Department of Computing, Imperial College London, London, United Kingdom;
[b]Royal Brompton Hospital, Cardiovascular Magnetic Resonance Unit, London, United Kingdom;

ABSTRACT

The paper presents a technique for detecting detecting left atrium as well as the pulmonary veins of the left atrium by tracing out their centerlines. A vessel detection and traversal process is initiated from the venoatrial junctions. Pulmonary veins draining into the left atrium via these junctions are thus detected, also enabling the detection of the ostium. Ostial diameters are measured from the detected centerlines using a best-fitting ellipse. Quantitative validation of the techniques are reported on nine patient datasets. In only two of the datasets, mis-detections were identified. The ostial diameter measurements indicated an error of at most 5% in most of the cases. We envisage that the techniques presented will facilitate in planning the non-pharmacological treatment of atrial fibrillation using radio-frequency ablation therapy.

Keywords: Segmentation, Treatment Planning, Cardiac Procedures, Image-Guided Therapy

1. INTRODUCTION

Atrial fibrillation (AFib) is the most common superventricular arrhythmia and a major cause of morbidity. AFib is a condition related to an abnormally fibrillating heart. Random electrical impulses fired from dysfunctional locations other than the sinoatrial node, disrupts the normal sinus rhythm. This leads to an abnormal rhythmic contraction of the atria and ventricles. As a consequence, heart rates are abornmally high in AFib patients. In comparison to healthy adults with heart rates in the range of 50-100 bpm, AFib patients can experience heart rates in the range of 400-600 bpm.[1] Such high heart rates pose the risk of sudden cardiac death through heart failure

A common treatment is to ablate tissues circumferentially at venoatrial junctions, using radio-frequency energy.[2] In this non-invasive procedure, the conduction paths of the abnormal electric impulse, originating from the pulmonary veins (PV), are blocked by creating circular lesions around the ostia. This interrupts the electric connection between the pulmonary vein and the left atrium. The lesions are created using a flexible surgical probe with a catheter at its tip. The catheter applies high radio-frequency (RF) energy for ablating tissues, thereby destroying its electrical conductance properties.

Pre-planning the ablation treatment is cruicial for successful procedures.[3] Knowledge of how many PV are present, and their ostia (opening) locations, is important to ensure that all ostia are ablated. Furthermore, ostial orientation and their diameters are important indicators of possible post-ablation stenosis and a determinant of catheter size. The presented techniques on automatic PV detection reduces the time and effort spent on ablation planning. It also reduces the risk of missing a PV for ablation, and some institutions now prefer to ablate all ostia to prevent the development of recurrent AFib.[3] Furthermore, automatic ostial diameter and circumference measurements increases the accuracy of these important surgical parameters.

Further author information: (Send correspondence to R. Karim)
R. Karim: E-mail: rkarim@imperial.ac.uk

2. RELATED WORK

Most previous work related to cardiac segmentation have focused on the left and right ventricles, except for the four-chamber heart model in Lorenz et al.,[4] Ecabert et al.[5] and Zheng et al.[6] Although Zheng et al.[6] models other structures apart from the chambers, such as atria-ventricular valves and the ventricular septum, most do not explicitly model the pulmonary vein drainages of the left atrium. Lorenz et al.[4] models the atrium and pulmonary vein drainages with a single model, and it is unclear if this is sufficient to capture the differing degrees of variation in the two structures. Lötjönen et al.[7] describes a 3D statistical shape model of the atria, but does not include the drainages. Vessel segmentation has been studied extensively, and some notable works include Sato et al.,[8] Frangi et al.,[9] Aylward et al.[10] and more recently McIntosh et al.[11]

Some of the previous research focuses on the segmentation of the left atrium for AFib. Berg et al.[12] build a mean surface model from example shapes. Each unseen instance then undergoes a simple thresholding step, and an iso-surface triangulation of the resulting volume is obtained. The mean model is then surface adapted to the triangulated surface of the unseen instance. The technique requires a good initialization. Also, it is difficult to confidently represent the amount of anatomical variation reported[13] using a single mean model. A watershed transform technique was proposed by Cristoforetti et al.[14] where the left atrium is segmented based on six different tissue classes, with the six marker positions interactively selected by the user. The segmentation is further refined using a post threshold-based segmentation step. A pure data-driven technique was proposed by John et al.[15] They use a region split-and-merge approach, whereby connected regions between the atrium and other structures are exploited. These connections are frequently narrow. Regions are split strategically across narrowings and then merged later on within non-narrow regions yields the segmented atrium. Our earlier work on left atrium segmentation[16] was similar to this technique. Although, these techniques produce the segmented atrium, further segmentation becomes necessary for extracting and measuring the PV during AFib ablation planning.

3. METHOD

3.1 Left atrium segmentation

The images acquired for this study are contrast-enhanced MRA images, where scans are acquired before and after the injection of the contrasting agent. Tissues which do not change after contrast-injection can be removed by subtracting the post- from the pre-MRA scans. The next step is to extract the left atrium (LA) blood pool. A simple region growing approach is used. The thresholds are automatically selected using the Otsu method.[17] A seed point is placed inside the atrium and an interactive bounding box is used to limit the growing region to stay within a region of interest. The blood pool extracted using region growing, will contain surrounding connected structures such as the ascending aorta and pulmonary arteries. These connections are artifacts caused by the partial volume effect.

Any surrounding structures can be removed using a LA segmentation technique. We use the one described in Karim et al.[16] This technique exploits the fact that the left atrium is only connected to other structures through narrowings manifested mostly by the partial volume effect. The extracted blood pool is subdivided into regions, where each region are the catchment basins of the local maximums of the Euclidean distance transform image. The Euclidean distance transform is computed on the binary LA blood pool. These subdivisons are later merged to obtain the left atrium. At this stage, what remains is the segmented LA along with the PV. Occasionally, there will also be remnants of pulmonary artery voxels.

3.2 Atrial body segmentation

The segmented left atrium will contain voxels belonging primarily to two tissue classes: the central atrial body and the pulmonary veins. We use the method described in Karim et al.[16] to segment the atrial body. The method is based on evolving surfaces using level set methods.[18] It is essentially a two-step process, where in the first step an initial surface *under-estimating* the atrial body size is obtained. This surface is then further evolved in a final step to give the final atrial body surface. The speed functions used in the two steps are different. In the first step, the Euclidean Distance (ED) transform of the left atrium segmented binary image is used. Starting from an initial small sphere placed at the center of the atrial body, the surface evolves under the ED transform

speed image. Here, speed values are mapped directly from ED values using a sigmoid which maps ED values to the range [-1,1]:

$$S = \frac{1}{1 + e^{-(\frac{d-\beta}{\alpha})}} \tag{1}$$

where d is the euclidean distance value. The evolving surface stops well before the atrial body boundary and venoatrial junctions. There is no leakage through these regions as these are usually within close proximity of edge voxels. The ED transform, and thus the speed, are small in the neighborhood of edge voxels, causing the propagation to slow down. This first step, although produces an under-segmentation, allows us to obtain an approximate shape of the atrial body.

In the second step, the surface obtained from the first step is further evolved. A second speed image is used which allows it to evolve relatively freely and only stops it from crossing the image edge boundaries. Speed values can thus be mapped from the image gradient magnitude. However, prior to computing the gradient, we perform an anisotropic diffusion smoothing[19] of the left atrium image and preserve edge boundaries.

$$\tilde{I} = \Gamma(I) \tag{2}$$

where $\tilde{I}$ is the image smoothed with anisotropic diffusion Γ. In order to clamp speed values between 0 and 1, a sigmoid function S is used. A rapid drop in speed is also desired at edge boundaries and the sigmoid helps to achieve this. The image gradient magnitude $\nabla\tilde{I}$ is thus mapped to speed values using:

$$S = \frac{1}{1 + e^{-(\frac{\nabla\tilde{I}-\beta}{\alpha})}} \tag{3}$$

It is also important to note that a high curvature constraint is placed on the evolving front in the second step. This restricts it to its initial shape acquired in the first step. Consequently, any leaks through the venoatrial junction in this second step are also avoided.

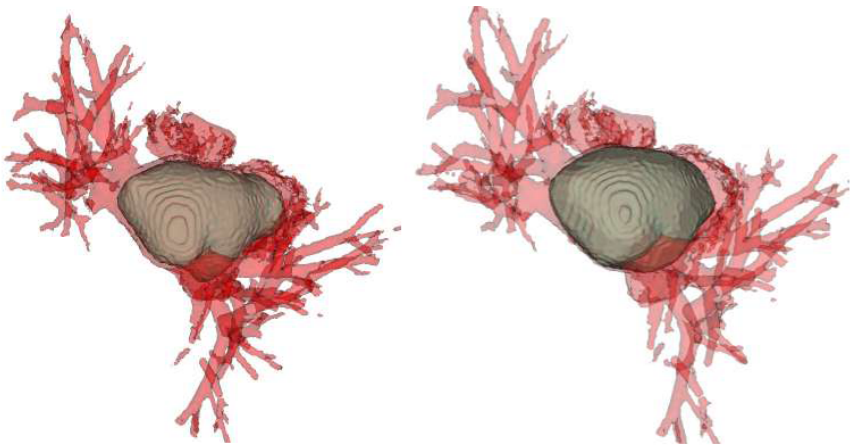

Figure 1. The above images show how the atrial body is obtained in two steps, with a different speed function being used in each step. The image on the left and right show results from first and second steps respectively.

3.3 Pulmonary vein centerline detection and tracking

After the extraction of the atrial body we are interested in finding the pulomonary veins which end in the atrial body. Our technique relies on the extraction of centerlines of tubular structures. With the atrial body segmented and removed, most of what remains are PV voxels. Since veins are tubular shaped, we can detect their centerlines. The centerlines serve two purposes: First, they identify the location and number of pulmonary vein branches emanating from the atrial body. Second, they allow the measurement of the ostial diameters.

3.3.1 Pulmonary vein centerline detection

We assume that vessels appear brighter than the background in contrast-enhanced MRI. *Ridges* are generated along the centerlines of vessels, when the image is convolved with a Gaussian kernel. These ridges are local maximums in at least one direction. Ideally, for the ridge to be along the centerline, the width of the smoothing kernel must equal the vessel's diameter. Thus, if the vessel is viewed as a 3D surface, the responses to the smoothing filter, generate 1D maximum convexity height ridges along the centerline. These intensity ridges can be detected and tracked. An excellent discussion on this topic can be found in Eberly et al.[20]

We start by computing a *vesselness* measure for each voxel within the LA segmented image. This can be accomplished using a vesselness filter.[9] Voxels within vessels give a high response to the filter compared to voxels outside vessels. The vesselness filter also computes, for each voxel, the optimal kernel widths or scales at which vesselness is maximal. For voxels within vascular structures, this width is the vessel diameter. Using this width information, we can now apply the Gaussian kernel of varying widths, to obtain the intensity ridges at the right scale. However, these ridge locations need to be detected. To this end, we employ a *ridgeness* measure for each voxel, similar to the one described in Aylward et al.[10]

Consider a continuous image function given by $I(x, y, z)$. If the intensity value is considered to be the height from zero, ridge points are locations where the image has a local maximum in the direction of principal curvature of $I(x, y, z)$. Using this criterion, the second derivatives at a point (x, y, z) can be used to identify ridge points. The Hessian matrix H, which captures second derivative in higher dimensions, can be analyzed to determine ridgeness at a point:

$$H = \begin{bmatrix} \frac{\partial^2 I}{\partial x^2} & \frac{\partial^2 I}{\partial x \partial y} & \frac{\partial^2 I}{\partial x \partial z} \\ \frac{\partial^2 I}{\partial y \partial x} & \frac{\partial^2 I}{\partial y^2} & \frac{\partial^2 I}{\partial y \partial z} \\ \frac{\partial^2 I}{\partial z \partial x} & \frac{\partial^2 I}{\partial z \partial y} & \frac{\partial^2 I}{\partial z^2} \end{bmatrix} \tag{4}$$

It is well known, that for a point to be on a 1D ridge of an N-D surface, $N - 1$ eigenvectors of the Hessian H of I at (x, y, z) must have negative eigenvalues.[9] Thus, given $\lambda_1, \lambda_2, \lambda_3$ are ordered eigenvalues of H with $|\lambda_1| \leq |\lambda_2| \leq |\lambda_3|$, at a ridge point we have:

$$\lambda_1 \leq \lambda_2 < 0 \tag{5}$$

The corresponding eigenvectors v_1 and v_2 are normal to the ridge, with v_3 tangent to the ridge. Based on this notion, also at a ridge point, the projection of the image gradient ∇I onto the two directions v_1 and v_2 normal to the ridge, must be zero:

$$v_1 \cdot \nabla I = 0 \text{ and } v_2 \cdot \nabla I = 0 \tag{6}$$

Using Eq. 6, a ridgeness function $J(x, y, z)$ can be defined over the image domain as:

$$J(x, y, z) = (v_1 \cdot \nabla I)^2 + (v_2 \cdot \nabla I)^2 \tag{7}$$

J is minimal along the 1D height ridge (intensity ridge) of a 3D surface. Our objective now is to use a minimization scheme to search for local minimums of this ridgeness function. By locating these local minimums, we will have located the vessel centerlines.

3.3.2 Automatic Seed Selection

Normally, four or more PVs drain into the LA. These veins are spatially located around the atrial body. The neighborhood of the venoatrial junction are good locations to start the vessel tracking process, and thus our seed points. Furthermore, seed points with high vesselness have greater chances of lying close to the centerline. However, prior to selecting seeds, these venoatrial junctions must be identified. To determine these regions, we threshold voxels of the left atrium, based on their distances from the segmented atrial body. For this, we compute for each LA voxel, the distance to the atrial body. This can be accomplished with a simple ED transform:

Assume two subsets in the image space I: Left atrium (LA) and atrial body (AB) where $AB \subset LA \subset I$. We define a set $\overline{AB}$ containing voxels *not in* AB:

$$\overline{AB} = I \backslash AB \tag{8}$$

Let $edt(.)$ denote the ED transform. We can thus compute $edt(\overline{AB})$ which gives a distance map for the shortest distance to the atrial body surface. Applying the LA as a mask on the distance map $edt(\overline{AB})$, we get, for each LA voxel, the distance to the atrial body. This distance map can now be used to judge which voxels are closest to the atrial body and thus in the neighborhood of venoatrial junctions.

We define three criteria for voxels to qualify as seeds:

1. They must be contained in the subset $LA - AB$.
2. They must lie within a fixed distance ϵ from the atrial body.
3. They must yield high responses to the vesselness filter.

There will be many voxels which satisfy these criteria, but we only randomly select 5% of the seeds.

3.3.3 Pulmonary Vein Tracking

Given that local minimums of the ridgeness function lie within the PV centerline, each PV branch emanating from the atrial body can be traversed using an iterative scheme. From each seed point, the ridgeness function J of Eq. 7 is minimized by employing a simple hill-descent approach. We walk along the direction of maximum descent by exploring a seed's 26-neighborhood. To estimate J at sub-voxel locations, a cubic B-spline interpolation is used. Once, at a ridge point P_0, we begin our ridge traversal process. Ridge traversal is an iterative process whereby at each iteration i we seek to move to the next ridge point P_{i+1}. Since, the third eigenvector v_3 of Eq. 5 approximates the vessel tangent direction, we utilize this to move a small number of steps in the direction of the vessel tangent. However, this may bring us to a point which may not necessarily be on the ridge. But, we can easily get back on the ridge by minimizing the ridgeness function J once again at that point. This iterative process is illustrated in Fig. 2.

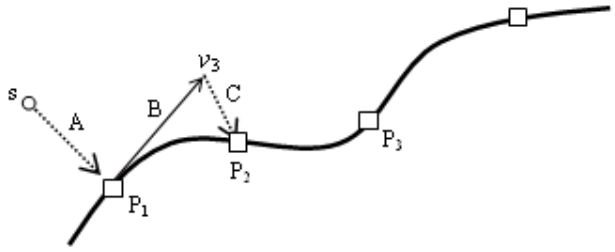

Figure 2. The figure shows the iterative steps involved in traversing a vessel represented by the curve. Step A - Starting from a seed point s, a local minimum of J is searched and found yielding the first point P_1 traversed on the vessel. Step B - At P_1, the vessel direction v_3 is computed, and a small distance is moved along this direction. Step C - Re-minimize J at this location to fall back on a new vessel point P_2.

It is important to specify the termination conditions for this scheme. As a precaution, we want the process to terminate once it is outside the segmented atrium or inside the atrial body. In addition to this, as sub-voxel vessel centerline positions are detected, their immediate neighborhood is marked as visited. When the traversal process encounters these visited locations, it is stopped. However, the traversed points are not outrightly rejected. If a significant length (i.e. above a threshold) of vessel was traversed before hitting a visited voxel, it is retained and marked as a vessel segment.

3.3.4 B-spline fitting of centerline points

The centerline points detected are often noisy, and it is beneficial to fit each detected segment with a B-spline curve.[21] A parametric B-spline curve with $n+1$ controlled points $\{\mathbf{Q}_i\}_{i=0}^{n}$ is given by:

$$P(t) = \sum_{i=0}^{n} N_{i,k}(t)\mathbf{Q}_i \tag{9}$$

where the basis functions $N_{i,k}(t)$ are given by:

$$N_{i,0}(t) = \begin{cases} 1, & t_i \leq t < t_{i+1} \\ 0, & \text{otherwise} \end{cases}$$

$$N_{i,k}(t) = \tfrac{t-t_i}{t_{i+k}-t_i} N_{i,k-1}(t) + \tfrac{t_{i+k+1}-t}{t_{i+k+1}-t_{i+1}} N_{i+1,k-1}(t)$$

Let a detected segmented of centerline points be denoted by $S = [\mathbf{s}_1\, \mathbf{s}_2 \ldots\, \mathbf{s}_m]^T$. In order to fit a B-spline curve through these points we look to minimize the scalar energy function E:

$$E(Q) = \frac{1}{2} \sum_{i=0}^{m} \left| \sum_{j=0}^{n} N_{j,k}(t_i)\mathbf{Q}_j - \mathbf{s}_i \right|^2 \tag{10}$$

where $Q = [\mathbf{Q}_1\, \mathbf{Q}_2 \ldots\, \mathbf{Q}_n]^T$ is a collection of unknown control points for the B-spline curve. By setting the partial derivatives of E to be zero, the set of control points Q that minimze this energy can be found. The number of control points for the fitting spline can be set to be a percentage ($\sim 10\%$) of the number of centerline points being fitted. For small segments, the number of control points is fixed.

3.4 Measuring Ostial Diameters

The Ostium size and location are important determinants of catheter size and post-ablation stenosis. The detected PV centerlines are good locations to measure the ostial diameters from. Moreover, an interactive perpendicular plane can move along this centerline and report the diameter at the desired location. This is useful for assessing post-ablation stenosis.

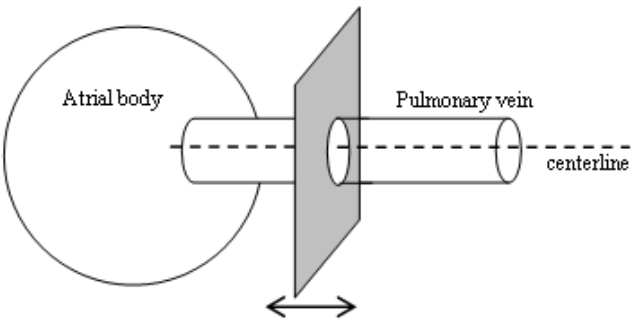

Figure 3. Ostial diameters are measured measured in the plane (in shaded grey) that can move perpendicular to the detected vessel centerline of this phantom model. An ellipse fitted to the intersecting region border is used to report the diameter.

3.4.1 Ellipse fitting of Pulmonary Vein cross-section

To measure the ostial diameter, we use our least-squares B-spline curve approximation for the centerline. A plane can be drawn at each sampled point $\mathbf{c}_i$ of the B-spline curve, with its normal being $\mathbf{c}_i - \mathbf{c}_{i+1}$. This can be considered to be a good approximation for the plane perpendicular to the vessel axis. The plane obliquely intersects the PV, and the intersection is simply a PV cross-section. Points on the boundary ∂P of this intersection are sampled, and a 2D ellipse can be fitted using a least-squares approach.

Consider the sampled points on boundary ∂P to be $\{\mathbf{P}_i\}_{i=1}^m$. An ellipse oriented arbitrarily can be represented using the following parameters: its center $\mathbf{C} = (x_0, y_0)$, an orthonormal matrix R representing its orientation, and $D = diag(1/a^2, 1/b^2)$ where a and b are the half-lengths of its major and minor axes. Fitting an ellipsoid then becomes an energy minimization problem:

$$E(\mathbf{C}, R, D) = \sum_{i=1}^{m} L_i \tag{11}$$

where L_i is the distance of the boundary point P_i to the ellipse with parameters $(\mathbf{C}, R, D)$. The major and minor-axes of the ellipse give a good estimate of the ostial diameter. In order to improve on this estimate, we measure several such diameters along the B-spline, by moving a small number of steps forward and backward along the spline. The average over all diameters is taken.

The circumference of the ostium is also of importance as it indicates the size of the catheter required for ablation. It is also a good indicator of the distance required to ablate. Also, some institutions now report the PV size in terms of their circumferences.[22] It can be estimated by adding up the distances between sampled boundary points $\{\mathbf{P}_i\}_{i=1}^m$. The true circumference C is given by adding infinitesimal segments on the boundary:

$$C = \lim_{k \to \infty} \sum_{i=0}^{k} |\mathbf{P}_i - \mathbf{P}_{i+1}| \tag{12}$$

where k are the number of points sampled on the boundary ∂P. Measuring the circumference using this method is more accurate than measuring them manually.

4. RESULTS

The data collected are MR angiography scans of 9 different patients. The imaging protocols are heterogeneous with different capture ranges and resolutions. Each volume may contain 80-100 slices, with the slice resolution being in the order of 300×300 pixels. The slice thickness is 1.3 mm. There was a significant amount of anatomic variability between the datasets, as can be seen in the surface reconstructions in Fig. 4. Following a non-rigid registration[23] of the pre- and post-MRA scans, they are subtracted to obtain only soft tissues. An anisotropic diffusion[19] smoothing step removes image noise whilst preserving image boundaries. The left atrium is next segmented followed by a segmentation of the atrial body. The vessel centerlines are extracted from the 9 datasets.

The results are validated, taking into consideration the clinical relevance of this detection process. For a clinician, the number of pulmonary veins draining into the atrial body is of more interest than their centerlines. We thus, report our results based on the number of pulmonary veins for which the centerlines were traced successfully. We compare these against a clinician's observations in Table 1.

Table 1. Table shows the number of pulmonary veins detected in each of the 9 patients, based on an expert's observation versus our automatic centerline technique

	P1	P2	P3	P4	P5	P6	P7	P8	P9
Expert	4	3	4	4	3	3	3	4	4
Automatic	4	3	4	6	3	3	3	2	4

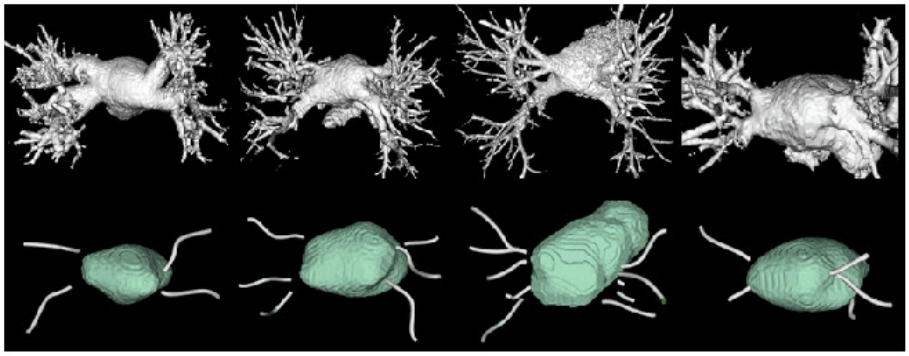

Figure 4. The upper row of images show the segmented left atria. The lower row shows the corresponding pulmonary vein centerlines detected and drawn out using best-fit cubic B-spline curves. Also, in the lower row are the segmented atrial bodies.

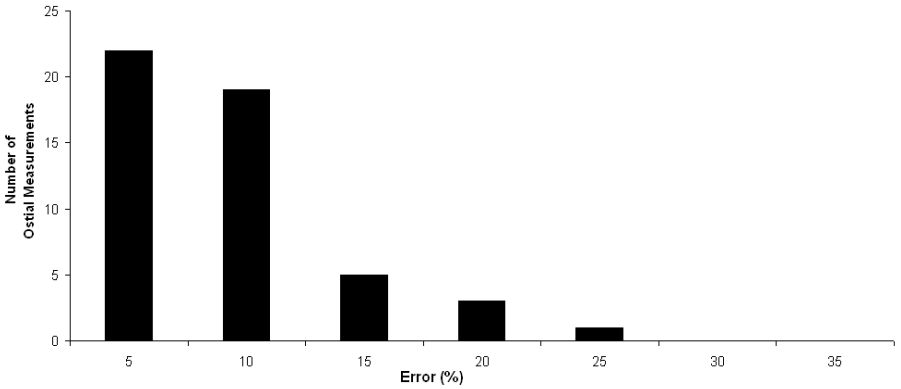

Figure 5. Histogram representation of the percentage error in ostial diameter compared against measurements of an expert radiologist. Each bin is 5% wide

Ostium measurements are usually taken on or within 5 mm of the venoatrial junction.[3] We validated our diameter measurement technique on 25 different ostia. A total of 50 measurements were taken at an average of 2 per ostium. In the histogram in Fig. 5, we report how our automatic diameter measurements compared against an expert radiologist's measurements. The percentage error, expressed as a percentage of the expert measurement, indicates the extent to which our results deviate from expert measurements. A little less than half of the measurements taken had a percentage error of no more than 5%, as indicated by the modal bin of the histogram.

The results indicate that the methods proposed are robust and potentially beneficial for ablation planning. The PV centerline detection can detect the number of PV branches draining into the left atrium. The detection is fast, and the entire process takes less than 3 minutes on a 2.0 Ghz machine. In addition to this, there is no user interaction required for the centerline detection step. A simplified visual of the atrial body and its PV branches is presented to the user, removing the un-wanted PV peripheries. This makes ablation planning easier.

For ostial diameters, results show close agreement with an expert observer. 5 out of 50 measurements taken had a percentage error of more than 20%. This is mostly near severely noisy segments of vessels, where the approximating spline can be expected to yield measuring planes that are not perfectly perpendicular to the true vessel axis. This can be easily rectified by interactively adjusting the plane, a feature which is available in our system. However, we have reported these results without the rectifications.

5. DISCUSSION

We believe that our approach can provide important information for planning the treatment of atrial fibrillation. Nevertheless, our method has some limitations. The ridgeness function J of Eq. 7 is minimized at each iterative

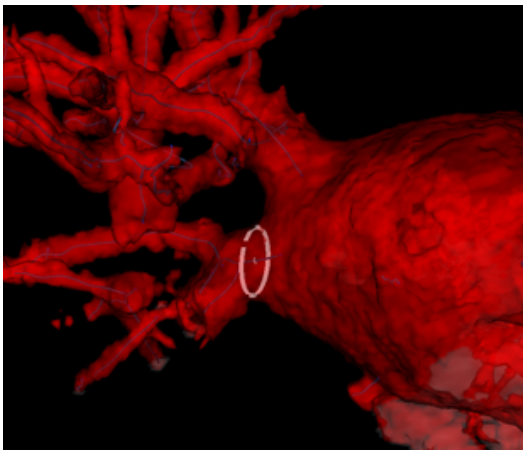

Figure 6. An iso-surface rendering of the segmented left atrium with a low opacity value to allow to see through. An ellipse fits to the pulmonary vein to measure its diameter automatically.

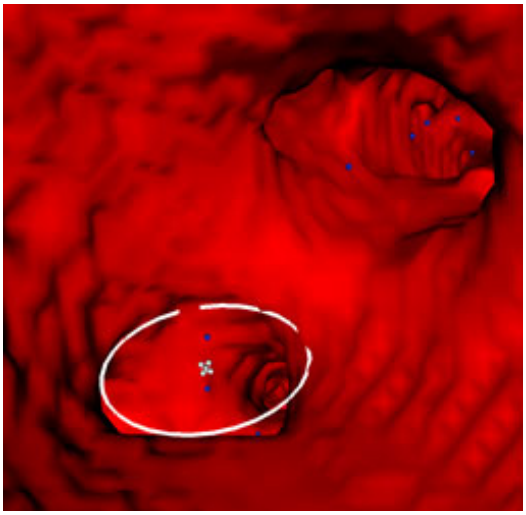

Figure 7. An endoscopic view of two ostia, with the best-ellipse fit (for measuring diameters) which can be seen drawn in the figure.

step of PV traversal. The local minimum is identified using a hill-descent approach. In 3D space, points around the neighborhood of a local minimum of a function act as basins. Any points lying within this neighborhood will converge to the same local minimum. The same is true for any N-D function. This makes our step sizes along the vessel direction an important factor for making the traversal process work. Any step size not large enough to surpass the local basin will make no traversal progress, as it will repeatedly converge to the same local minimum and thus the same vessel centerline point. Too large a step size, on the other hand, can cause traversal to exit vessels. This is more common within small vessels. This makes traversing small vessels (< 2 mm) rather difficult. Nevertheless, in ablation planning, the PV branches emanating from the atrial body are of more interest and these are easily tracked using our proposed method.

There are no currently imposed conditions on the direction the traversal process should take at a vessel bifurcation. The process is led to a branch directed by the minimization step. We expect the neglected branches to be detected subsequently from new seeds within them. However, if no seed is selected within a neglected branch, it will go undetected. This may be unlikely, although seed selection is a random process. Currently, only 5% of the voxels that satisfy the seed criteria listed in section 3.3.2 are selected as seeds. Raising this threshold level can ensure more seeds, and increase the probability of having at least a single seed within every branch.

6. CONCLUSION

Left atrium segmentation is an important segmentation problem.[3] It is of great interest in the planning of patient-oriented ablative treatment of AFib. The location and number of PVs draining into the left atrium are important for determining areas of ablation. In addition to this, ostial diameter and circumference are determinants of catheter size, post-ablation stenosis and for reporting the PV size. A technique for extracting PV centerlines and measuring ostial has been presented. To our knowledge, this is the first pulmonary vein and ostium detection technique of its kind.

The major contribution of this work is the detection of pulmonary veins of the left atrium. Also included, is an ostial diameter and circumference measurement technique. The Pulmonary vein centerline detection technique presented in this paper was able to detect the pulmonary veins in most of the patient data sets we have tested. Furthermore, the ostial diameters measured from the centerlines using ellipse-fitting, showed errors of no more than 10% in the majority of measurements taken.

REFERENCES

[1] Nattel, S., "New ideas about atrial fibrillation 50 years on," *Nature* **415**(6868), 219–226 (2002).

[2] Hebe, J., Hansen, P., Ouyang, F., Volkmer, M., and Kuck, K., "Radiofrequency Catheter Ablation of Tachycardia in Patients with Congenital Heart Disease," *Pediatric Cardiology* **21**(6), 557–575 (2000).

[3] Cronin, P., Sneider, M., Kazerooni, E., Kelly, A., Scharf, C., Oral, H., and Morady, F., "MDCT of the Left Atrium and Pulmonary Veins in Planning Radiofrequency Ablation for Atrial Fibrillation: A How-To Guide," *American Journal of Roentgenology* **183**(3), 767–778 (2004).

[4] Lorenz, C. and Berg, J., "A comprehensive shape model of the heart," *Medical Image Analysis* **10**(4), 657–670 (2006).

[5] Ecabert, O., Peters, J., and Weese, J., "Modeling shape variability for full heart segmentation in cardiac computed-tomography images," in [*Proceedings of SPIE*], **6144**, 61443R, SPIE (2006).

[6] Zheng, Y., Barbu, A., Georgescu, B., Scheuering, M., and Comaniciu, D., "Four-Chamber Heart Modeling and Automatic Segmentation 3D Cardiac CT Volume Using Marginal Space Learning and Steerable Features," *IEEE transactions on medical imaging* **27**(11), 1668 (2008).

[7] Lötjönen, J., Kivistö, S., Koikkalainen, J., Smutek, D., and Lauerma, K., "Statistical shape model of atria, ventricles and epicardium from short-and long-axis MR images," *Medical Image Analysis* **8**(3), 371–386 (2004).

[8] Sato, Y., Nakajima, S., Shiraga, N., Atsumi, H., Yoshida, S., Koller, T., Gerig, G., and Kikinis, R., "3D Multi-Scale Line Filter for Segmentation and," *Medical Image Analysis* **2**(2), 143–168 (1998).

[9] Frangi, A., Niessen, W., Vincken, K., and Viergever, M., "Multiscale Vessel Enhancement Filtering," *Lecture Notes in Computer Science* , 130–137 (1998).

[10] Aylward, S. and Bullitt, E., "Initialization, noise, singularities, and scale in height ridgetraversal for tubular object centerline extraction," *Medical Imaging, IEEE Transactions on* **21**(2), 61–75 (2002).

[11] McIntosh, C. and Hamarnerh, G., "Vessel crawlers: 3d physically-based deformable organisms for vasulature segmentation and analysis," in [*IEEE Conference on Computer Vision and Pattern Recognition*], **1**(1) (2006).

[12] von Berg, J. and Lorenz, C., "Accurate left atrium segmentation in multislice CT images using a shape model," in [*Proceedings of SPIE*], **5747**, 351, SPIE (2005).

[13] Marom, E., Herndon, J., Kim, Y., and McAdams, H., "Variations in Pulmonary Venous Drainage to the Left Atrium: Implications for Radiofrequency Ablation," *Radiology* , 230303031 (2004).

[14] Cristoforetti, A., Faes, L., Ravelli, F., Centonze, M., Del Greco, M., Antolini, R., and Nollo, G., "Isolation of the left atrial surface from cardiac multi-detector CT images based on marker controlled watershed segmentation," *Medical Engineering and Physics* **30**(1), 48–58 (2008).

[15] John, M. and Rahn, N., "Automatic Left Atrium Segmentation by Cutting the Blood Pool at Narrowings," *Lecture Notes in Computer Science* **3750**, 798 (2005).

[16] Karim, R., Mohiaddin, R., and Rueckert, D., "Left atrium segmentation for atrial fibrillation ablation," *Medical Imaging 2008: Visualization, Image-guided Procedures, and Modeling* **6918**(1), 69182U, SPIE (2008).

[17] Ostu, N., "A threshold selection method from gray-level histogram," *IEEE Transactions on Systems, Man and Cybernetics* **9**(1), 62–66 (1979).

[18] Sethian, J., [*Level set methods and fast marching methods*], Cambridge University Press (1999).

[19] Perona, P. and Malik, J., "Scale-space and edge detection using anisotropic diffusion," *IEEE Transactions on Pattern Analysis and Machine Intelligence* **12**(7), 629–639 (1990).

[20] Eberly, D., Gardner, R., Morse, B., Pizer, S., and Scharlach, C., "Ridges for image analysis," *Journal of Mathematical Imaging and Vision* **4**(4), 353–373 (1994).

[21] De Boor, C., [*A Practical Guide to Splines*], Springer (2001).

[22] Ahmed, J., Sohal, S., Malchano, Z., Holmvang, G., Ruskin, J., and Reddy, V., "Three-dimensional analysis of pulmonary venous ostial and antral anatomy: Implications for balloon catheter-based pulmonary vein isolation," *Journal of Cardiovascular Electrophysiolog* **17**(3), 251–255 (2006).

[23] Rueckert, D., Hayes, C., Studholme, C., Summers, P., Leach, M., and Hawkes, D., "Non-rigid Registration of Breast MR Images Using Mutual Information," *Lecture Notes in Computer Science* , 1144–1152 (1998).